
Article:
Kumar, Santosh, Isaacs, Mark A., Trofimovaite, Rima et al. (7 more authors) (2017) P25@CoAl layered double hydroxide heterojunction nanocomposites for CO2 photocatalytic reduction. APPLIED CATALYSIS B-ENVIRONMENTAL. pp. 394-404. ISSN: 0926-3373

https://doi.org/10.1016/j.apcatb.2017.03.006

Applied Catalysis B: Environmental 209 (2017) 394–404

Contents lists available at ScienceDirect

Applied Catalysis B: Environmental

journal homepage: www.elsevier.com/locate/apcatb

P25@CoAl layered double hydroxide heterojunction nanocomposites for CO_2 photocatalytic reduction

Santosh Kumar[a], Mark A. Isaacs[a], Rima Trofimovaite[a], Lee Durndell[a], Christopher M.A. Parlett[a], Richard E. Douthwaite[b], Ben Coulson[b], Martin C.R. Cockett[b], Karen Wilson[a], Adam F. Lee[a,*]

[a] European Bioenergy Research Institute, Aston University, Birmingham B4 7ET, UK
[b] Department of Chemistry, University of York, York YO10 5DD, UK

ARTICLE INFO

Article history:
Received 12 January 2017
Received in revised form 28 February 2017
Accepted 1 March 2017
Available online 2 March 2017

Keywords:
Photocatalysis
CO_2
Titania
Layered double hydroxide
Nanocomposite

ABSTRACT

Artificial photosynthesis driven by inorganic photocatalysts offers a promising route to renewable solar fuels, however efficient CO_2 photoreduction remains a challenge. A family of hierarchical nanocomposites, comprising P25 nanoparticles encapsulated within microporous CoAl-layered double hydroxides (CoAl-LDHs) were prepared via a one-pot hydrothermal synthesis. Heterojunction formation between the visible light absorbing CoAl-LDH and UV light absorbing P25 semiconductors extends utilisation of the solar spectrum, while the solid basicity of the CoAl-LDH increases CO_2 availability at photocatalytic surfaces. Matching of the semiconductor band structures and strong donor–acceptor coupling improves photoinduced charge carrier separation and transfer via the heterojunction. Hierarchical P25@CoAl-LDH nanocomposites exhibit good activity and selectivity (>90%) for aqueous CO_2 photoreduction to CO, without a sacrificial hole acceptor. This represents a facile and cost-effective strategy for the design and development of LDH-based nanomaterials for efficient photocatalysis for renewable solar fuel production from particularly CO_2 and water.

1. Introduction

Solar fuels production from CO_2 and water via artificial photosynthesis is considered a high risk/high reward strategy to deliver hydrogen and hydrocarbons as sustainable feedstocks to support global energy needs and security and mitigate anthropogenic climate change [1–3]. Semiconductor nanostructures are promising inorganic mimics of biological photocatalysts in this regard, offering diverse and tunable electronic, optical and physical properties [4–6]. Titania is the best known and most widely studied inorganic photocatalyst due to its abundance, long term photostability, established redox chemistry, UV absorption, and low toxicity [7]. The low cost and commercial availability of P25 titania from Evonik (previously Degussa) has resulted in its informal adoption by the scientific community as the prototypical photocatalyst against which to benchmark a wide range of light-driven reactions [8]. However, P25, a mixture of anatase and rutile nanocrystals, is a wide bandgap semiconductor and hence on its own offers limited potential for solar driven photocatalysis for which only 4% of incident radiation is UV light [8,9]. A range of approaches have been adopted to impart visible light absorption by titania, including band gap modification through doping or changing nanocrystal dimensions [9–12]. Alternatively, titania can be combined with narrow band gap semiconductors to extend light absorption into the visible region and hence improve photocatalytic efficiency [13,14] for e.g. photocatalytic H_2 evolution from water [15] or alcoholic solution [16] and organic pollutant degradation [14,17] through heterojunction formation.

CO_2 photoreduction presents additional challenges due to its weak adsorption over many inorganic photocatalysts, poor solubility in aqueous systems, common requirement for sacrificial hole acceptors to drive water oxidation, and slow multi-electron transfer kinetics necessary to yield CO, oxygenate (HCOOH or CH_3OH) or hydrocarbon (CH_4, C_xH_{2x-2}.) products [6,13,18]. A wide variety of porous, low dimensional, layered and/or hybrid inorganic nanomaterials have been investigated as photocatalysts for CO_2 reduction [19,20]. Layered double hydroxides (LDHs) are nanostructured, two dimensional layered solids of general formula $[M^{2+}_{1-x}M^{3+}_{x}(OH)_2]^{y+}(A^{z-})\cdot nH_2O$ where M^{2+} is commonly Ca^{2+}, Mg^{2+}, Ni^{2+}, Zn^{2+} or Co^{2+} and M^{3+} is Al^{3+} or Fe^{3+}, y = x, and

* Corresponding author.
E-mail address: a.f.lee@aston.ac.uk (A.F. Lee).

http://dx.doi.org/10.1016/j.apcatb.2017.03.006

A is a charge-balancing anion, typically a carbonate [21,22]. Their nanoporous architecture, earth abundant components, (relative) ease of scale-up, and tunable, narrow band gap semiconductor properties makes them attractive visible light photocatalysts [23–25]. However, pristine LDHs generally exhibit poor quantum efficiency under solar irradiation due to slow charge carrier mobility and high rates of electron-hole recombination [23,26]. Recent theoretical and experimental observations of conventional MgAl-, CoAl-, and ZnAl-LDHs suggest CoAl-LDH as an efficient photocatalyst for the oxygen evolution reaction due to the strong driving force for its photogenerated holes to overcome the overpotential for water splitting [27]. Considering that TiO_2 nanoparticles are good acceptors of photoinduced electrons [28,29], the construction of a heterojunction between P25 and CoAl-LDH would provide an effective way to drive both oxidation and reduction reactions without recourse to sacrificial agent, while the intrinsic basicity of the CoAl-LDH would enhance CO_2 adsorption at the composite photocatalyst surface. Dou et al. reported the construction of one such heterojunction arrangement, comprising large (250 nm) hollow TiO_2 nanospheres encapsulated by a CoAl-LDH shell, for photocatalytic water oxidation employing a sacrificial $AgNO_3$ electron acceptor [30]. Unfortunately, this material failed to drive both reduction and oxidation reactions without the sacrificial agent, and the heterojunction interfacial contact area was rather limited due to the core-shell morphology. There are a few other reports on TiO_2/LDHs heterostructures for photocatalysis, and those mostly for organic pollutant degradation (TiO_2/MgAl-LDH [31], TiO_2/ZnAl-LDH [32], TiO_2/CuMgAl-LDH [33], TiO_2/NiAl-LDH [34]) and O_2 evolution (TiO_2@ZnCr-LDH [24]) via water oxidation in the presence of sacrificial agent. The homogeneous dispersion of commercially available UV light-responsive P25 nanoparticles throughout a visible-light-responsive CoAl-LDH could significantly enhance the hetero/nanojunction contact area between semiconductor components, and thereby offer a low cost and efficient strategy to CO_2 photoreduction without recourse to a sacrificial agent.

Herein we report the one-pot hydrothermal synthesis of P25@CoAl-LDH nanocomposites for the aqueous phase photoreduction of CO_2 in the absence of sacrificial agents. A strong synergy is observed between semiconductor components, conferring high selectivity for CO, extended light absorption, suppressed electron-hole recombination, and a good quantum efficiency compared with P25 or CoAl-LDH. This synthetic strategy could be extended to a variety of photocatalytic applications for LDH nanocomposites including water splitting and depollution to address energy conversion and environmental issues.

2. Experimental

2.1. Material synthesis

Reagents $Co(NO_3)_2{\cdot}6H_2O$ (Sigma, 99%), $Al(NO_3)_3{\cdot}9H_2O$ (Sigma, 99%), P25 (Sigma), NH_4F (Sigma, 99%) and urea (Sigma, 99.9%) were used as received. All other chemical reagents used in this work were analytical grade and used without further purification. Hierarchical P25@CoAl-LDH nanocomposites were prepared by a modified one-pot hydrothermal method (employing a urea decomposition method previously used to prepare Au/NiAl-LDH oxidation catalysts [35]), with NH_4F as a structure-directing agent. Briefly, a known mass of P25 was dispersed in deionized water by ultrasonication (Elmasonic S100H, 5 min/550 W/50 Hz), to which 0.006 mols $Co(NO_3)_2{\cdot}6H_2O$, 0.002 mols $Al(NO_3)_3{\cdot}9H_2O$, 0.04 mols urea and 0.01 mols NH_4F were dissolved. The resulting suspension was aged in a 100 ml Teflon-lined autoclave at 120 °C for 24 h. The precipitate obtained was washed with deionized water until the washings were pH neutral, then dried overnight at 60 °C in vacuum to yield the final P25@CoAl-LDH material. The mass of P25 in the initial suspension was varied to produce P25@CoAl-LDH nanocomposites containing between 0 and 40 wt% titania. A similar method, omitting P25, was adopted to prepare a pure CoAl-LDH reference.

2.2. Characterization

Powder X-ray diffraction (XRD) patterns were recorded on a Bruker-AXS D8 ADVANCE diffractometer operated at 40 kV and 40 mA using Cu K_α radiation (0.15418 nm) between 10–80° in 0.02° steps. X-ray photoelectron spectroscopy was performed on a Kratos Axis HSi spectrometer with a monochromated Al K_α X-ray source operated at 90 W and magnetic charge neutralizer. Spectral processing was performed using CasaXPS version 2.3.16, with energy referencing to adventitious carbon at 284.6 eV, and surface compositions and peak fitting derived using appropriate instrumental response factors and common line shapes for each element. Bulk elemental analysis was performed by energy-dispersive X-ray spectroscopy (EDX) using an Oxford INCA EDX detector installed on a JEOL JSM-7000F field-emission SEM microscope operating at 20 kV accelerating voltage, which was used to image catalyst morphology. Nanostructure details were visualized on a JEOL JEM-2100 TEM microscope operating at 200 kV accelerating voltage. Porosimetry was performed through N_2 physisorption at 77 K using a Quantachrome NOVA 4000e porosimeter. Brunauer–Emmett–Teller (BET) surface areas were calculated over the relative pressure range 0.01–0.2. Pore size distributions were calculated by applying the BJH method to desorption isotherms for relative pressures >0.35. CO_2 chemisorption was performed on samples degassed at 120 °C using a He carrier gas on a Quantachrome ChemBET PULSAR™TPR/TPD instrument. Diffuse reflectance infra-red Fourier transform (DRIFT) spectra were obtained on samples diluted in KBr using a Thermo Scientific Nicolet iS50 FT-IR spectrometer. Diffuse reflectance UV–vis spectra (DRUVS) were measured on a Thermo Scientific Evo220 spectrometer using an integrating sphere and KBr as standard and samples diluted in KBr. Band gaps were calculated from Eq. (1) [36,37].

$$\alpha h\nu = A\left(h\nu - E_g\right)^{\frac{\eta}{2}} \quad (1)$$

where, α, E_g and A are the absorption coefficient, optical band gap energy and a proportionality constant respectively, while the variable η depends on the nature of the optical transition (direct or indirect) during photon absorption. The absorption coefficient α was calculated from the Kubelka–Munk function given in Eq. (2):

$$\alpha = \frac{(1-R)^2}{2R} \quad (2)$$

while E_g was estimated from a Tauc plot of $(\alpha h\nu)^{\frac{1}{2}}$ versus h ν from a tangent to the band edge, the exponent reflecting anatase TiO_2 and CoAl-LDH are indirect band gap semiconductors. Steady state photoluminescence (PL) spectra of samples were recorded on a F-4500FL spectrometer at an excitation wavelength of 380 nm. PL lifetime data were collected on an Edinburgh Photonics FLS 980 spectrometer using a picosecond pulsed LED light with an excitation wavelength of 380 nm.

2.3. Photocatalysis measurements

Photocatalytic CO_2 reduction was carried out at room temperature in a sealed 320 ml stainless steel photoreactor with a quartz window and a 300 W Xe light source. 50 mg of sample was dispersed in 5 ml of water by ultrasonication for 5 min and charged in the photoreactor. Prior to irradiation, the reaction mixture was purged with bubbling CO_2 at 1 bar for 2 h at 6 ml min^{-1} in the dark

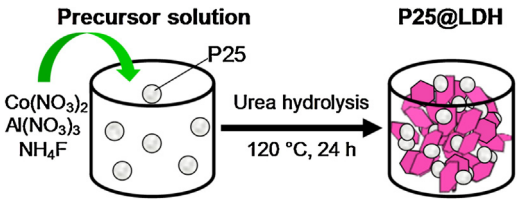

Scheme 1. Preparation route to P25 encapsulated hierarchical CoAl-LDH hetero/nanostructures.

to degas air from the solution and saturate with CO_2. The reaction mixture was subsequently continuously irradiated with UV–vis light using a 300 W Xe Toption Group. Ltd TOP-X300 lamp (spectral output shown in Fig. S1), and aliquots of the reaction mixture periodically withdrawn with a 1 ml air-tight gas syringe for analysis on a Shimadzu Tracera GC-2010 Plus chromatograph fitted with a Carboxen1010 (30 m × 0.53 mm × 0.1 μm) column with a He carrier gas and Barrier Ionization Detector. Liquid products were also analysed periodically from separate aliquots on an Agilent 1260 HPLC fitted with a Hi Plex column, however no carbon-containing liquid products were detected in this study. P25 was pre-dried in air at 200 °C for 4 h prior to use in reference experiments to remove trace carbonaceous residues, which resulted in small quantities of evolved CO and CH_4 during control experiments under nitrogen in the absence of CO_2. Selectivity for reactively-formed CO was calculated from Eq. (3) below:

$$\text{COselectivity}/\% = \frac{2N_{CO}}{2N_{CO} + 2N_{H_2}} x100 \quad (3)$$

where N_{CO} and N_{H2} are the yields of reactively-formed CO and H_2 respectively. Apparent quantum yields (AQYs) were calculated from Eq. (4) as follows [37]:

$$\text{AQY}/\% = \frac{\text{Number of reacted electrons}}{\text{Number of incident photons}} \times 100 \quad (4)$$

at 365 and 475 nm employing band pass filters, as detailed in the supporting information.

3. Results and discussion

The one-pot synthesis of the P25@CoAl-LDH nanocomposites is summarized in Scheme 1, and analogous to the report of Du et al. for Au@NiAl-LDH, is proposed to occur through the rapid precipitation of Al^{3+} cations accompanying urea hydrolysis resulting in $Al(OH)_3$ nucleation around P25 nanoparticles, and parallel complexation of Co^{2+} and F^- ions which regulates the availability of Co^{2+} ions in solution resulting in the subsequent slow dissolution of $Al(OH)_3$ and growth of CoAl-LDH platelets around titania.

The morphology of P25, CoAl-LDH and 20 wt% P25@CoAl-LDH were investigated by SEM and TEM. Fig. 1a and b shows that the 20 wt% P25@CoAl-LDH nanocomposite exhibits the sand rose structure typical of layered double hydroxides, comprising ~4–5 μm spherical agglomerates of two dimensional CoAl-LDH nanoplatelets approximately 20 nm thick and several hundred nanometers across (Fig. S2a). TEM revealed additional structural features, namely irregular nanoparticles spanning 20–50 nm indicative of P25 (Fig. S2b), uniformly dispersed throughout, and decorating, the nanoplatelets (Fig. 1c–e). Elemental EDX mapping confirmed a relatively high and uniform distribution of titania throughout the CoAl-LDH matrix (Fig. S2). High resolution imaging confirms existence of a well-defined titania- CoAl-LDH heterojunction interface, with lattice fringes consistent with the CoAl-LDH layer (0.55 nm) [24] and (001) plane of anatase TiO_2 nanoparticles (0.24 nm) [38].

Powder XRD confirmed that the nanocomposites contained both crystalline CoAl-LDH and P25 components for all titania loadings (Fig. S3). The CoAl-LDH was evidenced by reflections consistent with (003), (006), (009), (012), (018), (110), and (113), characteristic of the pure CoAl-LDH reference (PDF-#38-0487) with an interlayer spacing of 0.748 nm (d_{003}), indicating the presence of interlayer CO_3^{2-} and water [39], with additional reflections characteristic of anatase (PDF-#21-1272) and rutile (PDF-#21-1276) titania. Dimensions of both titania and CoAl-LDH crystallites were independent of titania loading (Table 1), confirming that the nanocomposite composition could be varied over a wide range (10–40 wt%) without altering the phase or morphology of either component. The measured TEM thickness of a cation layer in the reference CoAl-LDH was 0.55 nm; combining this with the theoretical ionic radius of CO_3^{2-} of 0.18 nm yields a predicted basal spacing (sum of a CoAl sheet and the interlayer gap) of 0.74 nm, consistent with that experimentally obtained by XRD of 0.75 nm for both the reference CoAl-LDH and the 20 wt% P25@CoAl-LDH nanocomposite. A physical mixture of P25 and CoAl-LDH reference materials in a 1:4 mass ratio (i.e. 20 wt% P25) exhibited an almost identical diffraction pattern to the equivalent nanocomposite, highlighting that P25 encapsulation did not affect the crystallinity of either component.

Surface properties of the P25@CoAl-LDH nanocomposites were subsequently explored by DRIFTS (Fig. S4), which confirmed the presence of vibrational bands at 3490 and 1560 cm^{-1}, identical to those observed for the CoAl-LDH reference, and consequently assigned to the O—H stretch and bending modes of interlayer water molecules, respectively, and additional bands at 1355 and 770 cm^{-1} likewise attributed to respective stretch and bending modes of interlayer CO_3^{2-} anions [39–41]. The P25 reference exhibited a strong band around 700 cm^{-1} associated with Ti—O stretches and bending modes, and a weak feature at 3300 cm^{-1} corresponding to the O—H stretch of physisorbed water [42]. Surface functionalities on the physical mixture mirrored those of the equivalent nanocomposite.

Nitrogen porosimetry of P25@CoAl-LDH revealed type II adsorption-desorption isotherms characteristic of macroporous materials (or non-porous materials possessing large interparticle voids) with H3-type hysteresis loops (Fig. S5). The magnitude of the hysteresis was inversely proportional to the P25 content, reflecting its primary origin in the CoAl-LDH component; according to IUPAC classification, H3 hysteresis loops arise from non-rigid aggregates of plate-like particles such as microporous clays [43]. Despite their evolving porosity, all nanocomposites exhibited similar BET surface areas around 55 $m^2\ g^{-1}$ (Table 1), with negligible difference between the 20 wt% P25@CoAl-LDH nanocomposite and a simple physical mixture of the two components in the same mass ratio.

Optical properties of DRUVS of the 20 wt% P25@CoAl-LDH nanocomposite and P25 and CoAl-LDH reference materials are compared in Fig. 2. P25 showed the expected strong absorption band in the UV centered around 300 nm and subsequent sharp cut-off >385 nm reflecting its extremely poor visible photoactivity, corresponding to an optical band gap of 3.20 eV (Fig. S6a). In contrast, the CoAl-LDH reference displayed two distinct absorption features, including a broad band in the visible region centered around 500 nm attributable to d–d transitions of octahedral Co^{2+} within the CoAl-LDH layer [44]. The d states of Co^{2+} are split into t2g

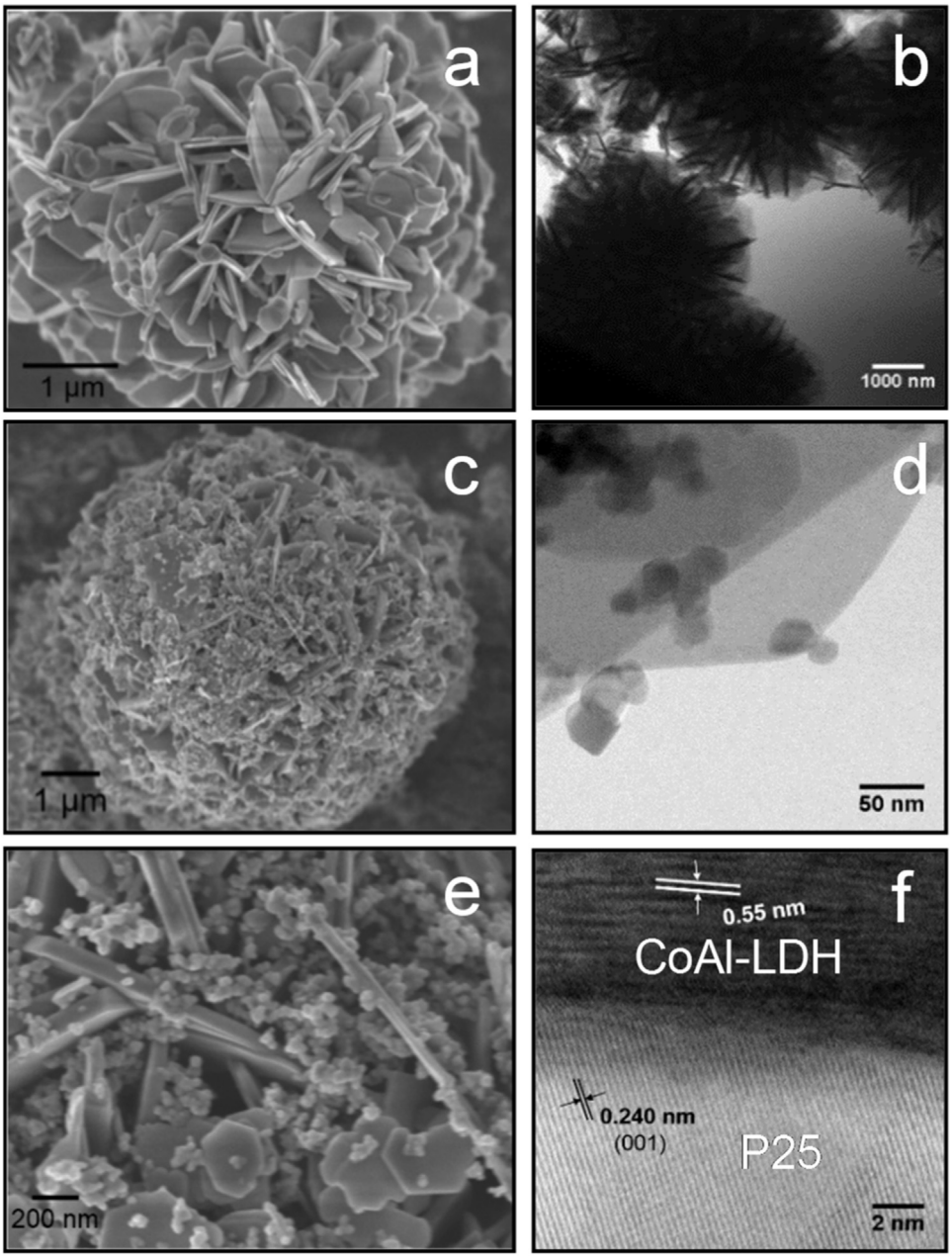

Fig. 1. Low resolution (a, c) SEM and (b, d) TEM, and (e) high resolution SEM, and (f) TEM images of pure CoAl-LDH and 20 wt% P25@CoAl-LDH, respectively.

Table 1
Physicochemical properties of P25@CoAl-LDH nanocomposites.

Material	Co:Al ratio[a]	P25[b]/wt%	Crystallite size[b] /nm		Surface area[c]/$m^2\ g^{-1}$	CO_2 capacity[d]/$\mu mol\ g^{-1}$
			LDH	P25		
CoAl-LDH	2.94:1	–	20	–	66	13
10wt%P25@CoAl-LDH	2.89:1	9	21	26(A), 37(R)	63	11
20wt%P25@CoAl-LDH	2.91:1	21	22	22(A), 34(R)	57	10
20wt%P25 + CoAl-LDH phy.mix	2.93:1	20	20	22 (A)34 (R)	60	8
30wt%P25@CoAl-LDH	2.87:1	29	22	24(A), 35(R)	53	8
40wt%P25@LDH	2.92:1	41	24	24(A), 38(R)	53	7
P25	–	–	–	22(A), 33(R)	54	5

[a] ICP.
[b] XRD (A = anatase, R = rutile).
[c] Porosimetry.
[d] Chemisorption.

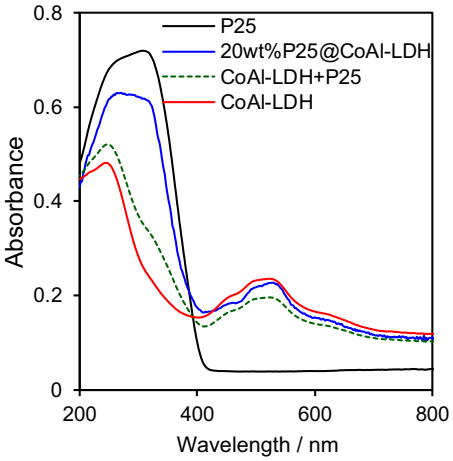

Fig. 2. DRUV spectra of 20 wt% P25@CoAl-LDH and P25 and CoAl-LDH reference materials. Spectrum of a physical mixture of 20 wt% P25 + CoAl-LDH shown for comparison.

and eg orbitals in an octahedral environment, with further splitting of t_{2g} and e_g orbitals due to spin–spin exchange interactions [45,46]. In ligand field theory, the ground state of Co^{2+} d^7 is $4T_{1g}$ (4F) and the first excited state is $4T_{1g}$ (4P). However there are three spin-allowed transitions, $4T_{2g} \rightarrow 4T_{1g}$ (F), $4A_{2g} \rightarrow 4T_{1g}$ (F) and $4T_{1g}$ (P) $\rightarrow 4T_{1g}$ (F) which give rise to the broad visible absorption band for CoAl-LDH in Fig. 2. The associated optical band gap for CoAl-LDH was 2.1 eV (Fig. S6b). The 20 wt% P25@CoAl-LDH nanocomposite exhibits features intermediate between its constituent components, with a prominent UV absorption due to P25 nanoparticles superimposed on the visible light responsive CoAl-LDH aggregates. Heterojunction formation is indicated by a shift to higher wavelength in the absorption cut off edge between the UV and visible regions relative to a 20 wt% P25 + CoAl-LDH physical mixture.

The electronic structure of the 20 wt% P25@CoAl-LDH nanocomposite was further investigated by XPS. Fig. 3 shows the resulting Co 2p and Ti 2p XP core level spectra, and those of the CoAl-LDH and P25 reference materials. The Co 2p spectra of the CoAl-LDH reference exhibited the expected spin-orbit split doublet (Fig. 3a), with $2p_{3/2}$ and $2p_{1/2}$ components at 780.68 and 796.93 eV binding energy respectively and satellites at 786.47 and 802.23 eV indicative of high-spin divalent Co^{2+} species within the CoAl-LDH layers [30,47]. Fig. 3b shows that the corresponding Ti 2p spin-orbit split doublet for the P25 reference, with $2p_{3/2}$ and $2p_{1/2}$ components at 458.37 and 464.20 eV respectively consistent with a Ti^{4+} oxidation state [48]. Similar electronic environments were observed for Co and Ti within the 20 wt% P25@ CoAl-LDH heterostructure, but with a small increase in the Co $2p_{3/2}$ binding energy (to 781.04 eV) and concomitant decrease in the Ti $2p_{3/2}$ binding energy (to 458.15 eV) relative to the two references. Quantitatively similar shifts were reported following the formation of core–shell nanocomposites between hollow TiO_2 nanospheres and an encapsulating CoAl-LDH shell [30], and are consistent with initial state binding energy changes arising from electron transfer from the CoAl-LDH to P25. Neither shift was evident in the Co or Ti 2p XP spectra for a physical mixture of P25 and CoAl-LDH, highlighting the unique nanocomposite electronic structure.

Valence band maximum (VBM) edge potentials for the CoAl-LDH and P25 references were also determined by valence band XPS (Fig. 3c and d) from the intercept of the tangent to the density of states at the Fermi edge as 1.35 eV and 2.83 eV respectively, in agreement with the literature [30,49]. These values can be used in conjunction with the preceding optical band gap energies to calculate corresponding conduction band maximum (CBM) potentials of −0.75 eV (CoAl-LDH) and −0.37 (P25) respectively. Band bending and charge transfer associated with heterojunction formation within 20 wt% P25@CoAl-LDH was explored by determining the valence band offset ΔE_{VBM} of the CoAl-LDH relative to P25 component, according to Eq. (5) [50,51]:

$$\Delta E_{VBM} = \left(E_{CL}^{Co} - E_{V}^{Co}\right) - \left(E_{CL}^{Ti} - E_{V}^{Ti}\right) + \Delta E_{CL} \quad (5)$$

where $\left(E_{CL}^{Co} - E_{V}^{Co}\right)$ is the energy difference between the Co $2p_{3/2}$ and VBM in the pure CoAl-LDH reference, $\left(E_{CL}^{Ti} - E_{V}^{Ti}\right)$ is the energy difference between the Ti $2p_{3/2}$ and the VBM in the P25 reference, and $\Delta E_{CL} = \left(E_{CL}^{Co} - E_{CL}^{Ti}\right)$ is the energy difference between the Co $2p_{3/2}$ and Ti $2p_{3/2}$ core levels (CLs) at the P25@ CoAl-LDH heterojunction. The resulting ΔE_{VBM} was 0.95 eV, indicating significant band bending due to heterojunction formation. The corresponding conduction band offset ΔE_{CBM} of the CoAl-LDH relative to P25 component was determined according to Eq. (6):

$$\Delta E_{CBM} = \left(E_{g}^{CoAl-LDH} - E_{g}^{P25}\right) - \Delta E_{VBM} \quad (6)$$

where $E_g^{CoAl-LDH}$ and E_g^{P25} are the band gaps of the references, 2.1 eV and 3.2 eV respectively, resulting in a ΔE_{CBM} of 0.15 eV. These energy levels and band offsets are depicted in Fig. 4a, and indicative of a type-II (staggered) band alignment at the P25@CoAl-LDH heterojunction, and the associated band bending before and after contact between the titania and CoAl-LDH components illustrated in Fig. 4b. This band alignment is considered advantageous for the transport of photogenerated charge carriers, which in this instance is expected to results in hole-rich CoAl-LDH layers and electron-rich P25 nanoparticles, i.e. a heterojunction promoting electron-hole separation.

Charge transport within the 20 wt% P25@CoAl-LDH was further probed through steady state and time-resolved photoluminescence (PL) spectroscopy following 380 nm excitation. P25 exhibited a single weak emission peak around 470 nm (Fig. 5a) arising from charge recombination on oxygen vacancies within titania [49,52], whereas the CoAl-LDH reference exhibited two emission peaks at 470 nm (strong) and 525 nm (medium) associated with ligand field transitions 4T2g → 4T1 g (F) and 4T1 g (P) → 4 T1 g (F) observed commonly in octahedral cobalt(II) compounds [46,53], similar to previous reports for Co-Al-LDHs [30,49]. The PL spectra of the nanocomposite was intermediate between the references, with the 470 nm peak intensity significantly lower than that of pure CoAl-LDH, while the 520 nm peak was extremely weak relative to a simple 20 wt% P25 + CoAl-LDH physical mixture, evidencing supressed electron–hole recombination [30,36]

Time-resolved PL spectroscopy provided additional insight into photogenerated charge carrier dynamics (Fig. 5b) from the resulting decay curves which were fitted with a biexponential function according to Eq. (7) below [46,54].

$$Fit = A + B_1 e^{\left(\frac{-t}{\tau_1}\right)} + B_2 e^{\left(\frac{-t}{\tau_2}\right)} \quad (7)$$

where A is a constant employed in the baseline correction, B_1 and B_2 are constants corresponding to non-radiative and radiative relaxation processes originating from the direct formation of free charge carrier and the indirect formation of self-trapped excitons respectively [55], τ_1 and τ_2 the corresponding decay lifetimes associated with the recombination of photogenerated holes and electrons, and t is time. The average charge carrier lifetime (τ) was calculated from Eq. (8) [54]:

$$\tau = \frac{B_1\tau_1^2 + B_2\tau_2^2}{B_1\tau_1 + B_2\tau_2} \quad (8)$$

Fitted parameters are summarized in Table 2 for the P25 and CoAl-LDH references and 20 wt% P25@CoAl-LDH, with χ^2 a measure of the goodness of fit and close to unity for all three samples indicating excellent agreement with experimental data (typical literature

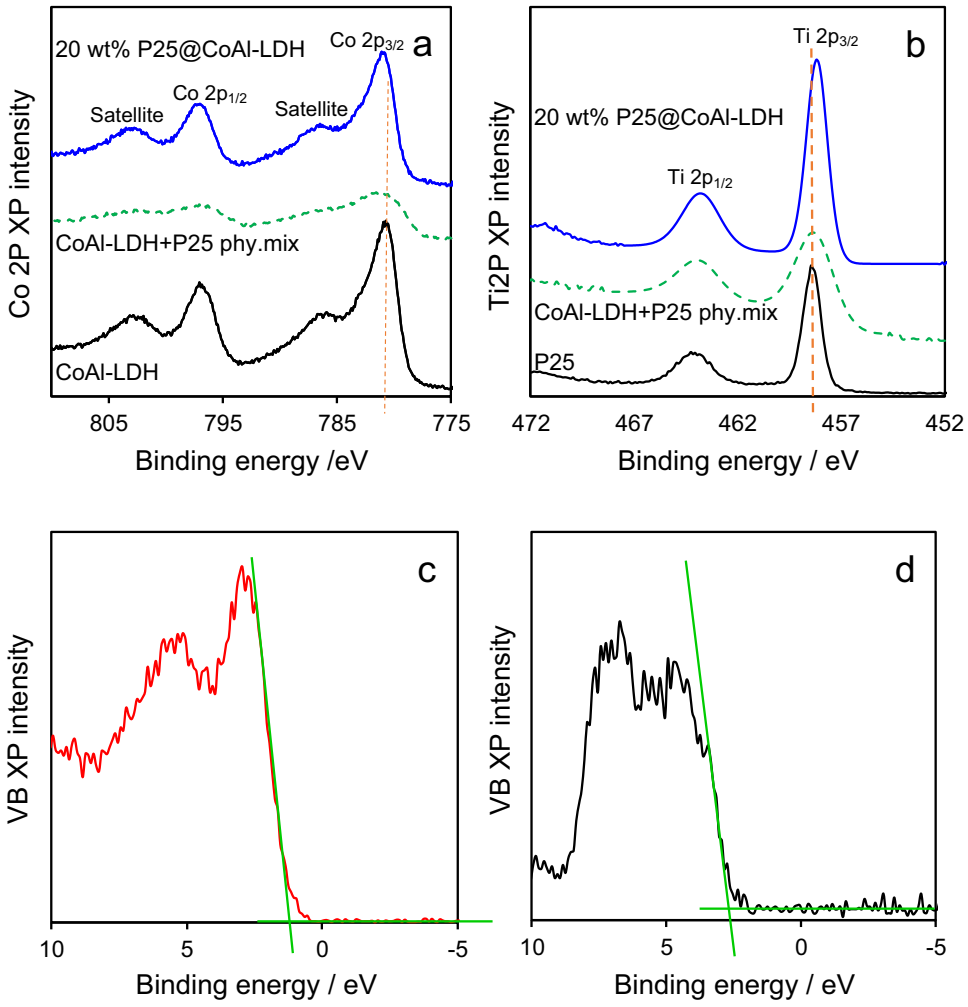

Fig. 3. (a–b) Core level and (c–d) valence band XP spectra of 20 wt% P25@CoAl-LDH and P25 and CoAl-LDH reference materials. Core level spectra of a physical mixture of 20 wt% P25 + CoAl-LDH shown for comparison.

Table 2
Fitted parameters from time-resolved PL spectroscopy of 20 wt% P25@CoAl-LDH nanocomposite for a 380 nm excitation wavelength.

Material	$\tau_{1\ /ns}$	$\tau_{2\ /ns}$	B_1	B_2	τ/ns	χ^2
P25	0.98	2.58	3190.45	609.52	1.50	1.17
CoAl-LDH	1.59	7.90	643.89	58.09	3.54	1.06
20wt%P25@CoAl-LDH	1.85	11.10	222.49	55.26	7.03	1.05
CoAl-LDH+P25	1.74	8.43	215.29	16.40	3.99	1.08

fits are 1.0–1.25 [46,54]). For 20 wt% P25@ CoAl-LDH, $\tau = 7.03$ ns, almost double that of CoAl-LDH (3.54 ns), five times longer than that of P25 (1.5 ns), and also much higher than that of a physical mixture of P25 and CoAl-LDH (3.99 ns), revealing significantly slower electron-hole pair recombination in the nanocomposite than any reference material, a synergy we attribute to the associated heterojunction between and charge trapping on the P25 and CoAl-LDH components. The values in Table 2 are comparable to literature reports of τ_1 and τ_2 of 0.3 and 4.5 ns for P25 [56] ($\tau = 1.16$ ns) and τ_1 and τ_2 of 0.4 and 1.5 ns for pure anatase [57], and τ_1 and τ_2 of 3.2 and 4.0 ns for a related NiFe-LDH [58] ($\tau = 5.5$ ns); it is interesting to note that composite formation between the latter NiFe-LDH and an amorphous layered g-C_3N_4 also prolonged the photogenerated charge lifetime τ to 8.6 ns [58].

The photocatalytic performance was determined of P25@CoAl-LDH nanocomposite for the aqueous phase CO_2 reduction under UV–vis irradiation in the absence of a sacrificial hole acceptor, which was compared with that of P25 and CoAl-LDH references (Fig. 6). In order to discount possible artefacts arising from carbon contamination and confirm water as the proton source [59], a number of control experiments were first performed in the absence of CO_2, H_2O, catalyst or light, which confirmed that all four elements were required to observe any reaction products (Fig. S**7**). Only three products were observed in all cases, CO, H_2 and O_2, with no hydrocarbons detected in either the gas or liquid phase. P25 exhibited the poorest photoactivity for CO_2 reduction or water oxidation, presumably reflecting fast charge carrier recombination, low CO_2 absorptivity and its conduction band maximum potential of −0.37 eV (Fig. 4), which is too low to drive $CO_2 + 2H + 2e^- \rightarrow CO + H_2O$ ($E^{00} = -0.53$ eV at pH 7) but sufficient to drive significant proton reduction to hydrogen (Fig. 6b). The CoAl-LDH reference by comparison produced appreciable CO and oxygen (Fig. 6a and c), reflecting its higher conduction band maximum of −0.75 eV and longer average charge carrier lifetime τ. All P25@CoAl-LDH nanocomposites evidenced a synergy between constituent semiconductor components, with superior CO and oxygen productivity to either reference material alone, or a 20 wt% P25 + CoAl-LDH physical mixture which exhibited only 0.84 μmol h^{-1} g^{-1} CO. Since the physicochemical properties of each component (phase, crystallite size, surface area, CO_2 chemisorption capacity and formal oxidation state) in the nanocomposites are identical to (or a simple average) of the reference materials, this synergy is attributable directly to heterojunction formation and the

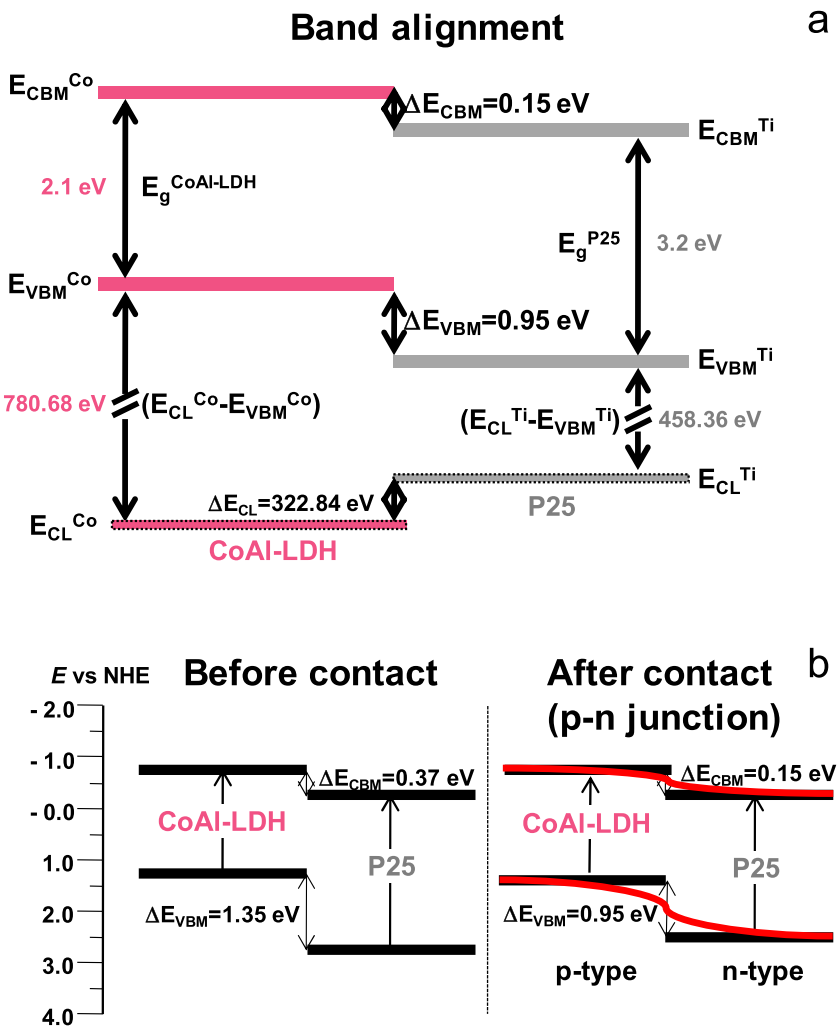

Fig. 4. (a) Band alignment and (b) band bending before contact and after heterojunction junction formation in 20 wt% P25@CoAl-LDH nanocomposite.

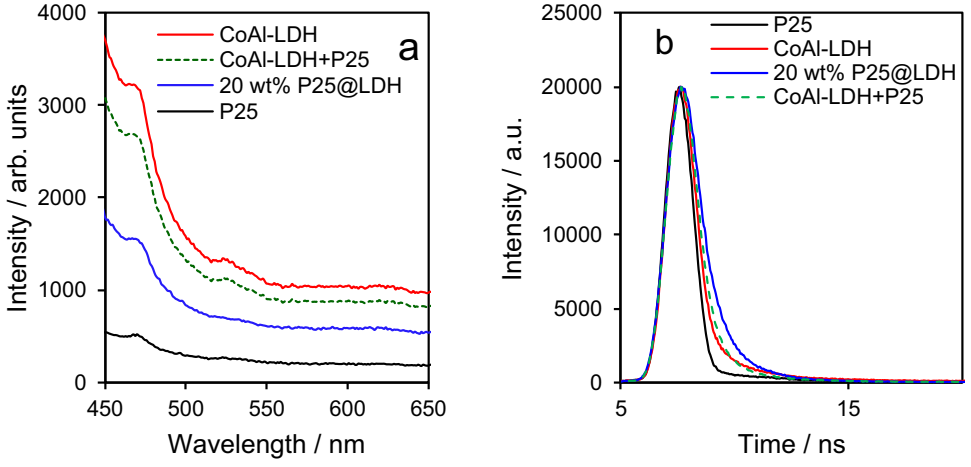

Fig. 5. (a) Steady state and (b) time-resolved PL spectra of 20 wt% P25@CoAl-LDH and P25 and CoAl-LDH reference materials following 380 nm excitation. Steady state and time-resolved PL of a physical mixture of 20 wt% P25 + CoAl-LDH shown for comparison.

associated spatial separation of electrons and holes and attendant slow recombination rate.

The P25@CoAl-LDH materials displayed a volcano dependence of CO_2 photoreduction performance on P25 content, with maximum CO and O_2 productivity, and a CO selectivity of 94% (Fig. S8) for 20 wt% P25@CoAl-LDH; this equated to a 2.5 and 5.5 fold increase in CO productivity relative to CoAl-LDH and P25 references. The CO:O_2 product stoichiometry was between 1.78:1 and 1.96:1 for all nanocomposites and CoAl-LDH reference, very close to the 2:1 stoichiometry expected if CO_2 photoreduction was the

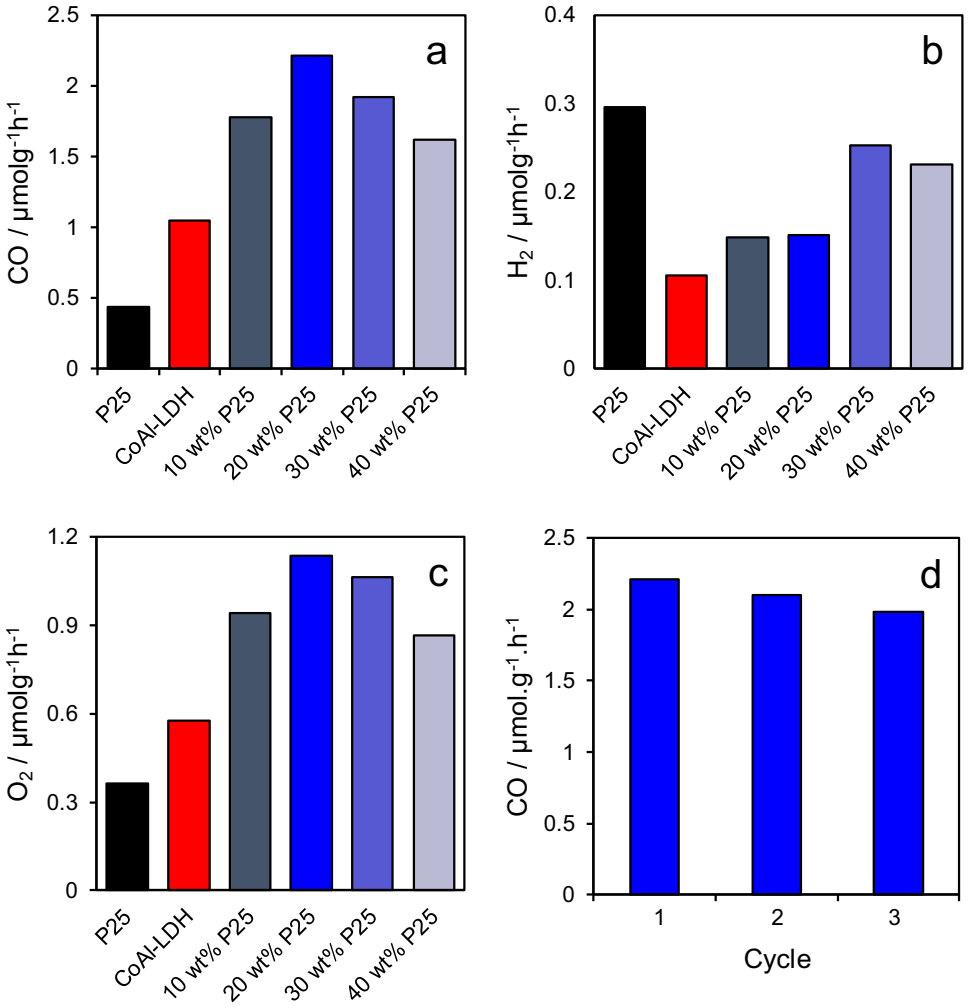

Fig. 6. (a) CO, (b) H_2 and (c) O_2 mass-normalized productivity averaged over the first 4 h aqueous phase CO_2 photoreduction over P25 and CoAl-LDH references and P25@CoAl-LDH nanocomposites under UV–vis irradiation. (d) Recycle reactions for 20 wt% P25@CoAl-LDH.

only catalytic process operating: CO_2 reduction to CO is a $2e^-$ process, in contrast to water oxidation which is a four electron process, $2H_2O \rightarrow O_2 + 4H^+ + 4e^-$, hence two CO molecules are formed for each O_2 molecule from water splitting. The exception is the P25 reference, for which significantly more oxygen was evolved than anticipated, reflecting a higher propensity for water oxidation consistent with the observed highest rate of H_2 production in Fig. 6b.

Synergy between the two semiconductors was further demonstrated by comparing CO productivity for the 20 wt% P25@CoAl-LDH under UV–vis versus visible light irradiation which yielded values of 2.21 versus 0.714 μmol h^{-1} g^{-1} respectively, highlighting the importance of hole generation on the P25 component through UV excitation (and subsequent transport to the LDH component hindering recombination with photoexcited electrons). Our CO productivities are significantly higher than literature reports for diverse inorganic heterostructure photocatalysts (Table S1), which span 0.25-1.74 μmol h^{-1} g^{-1} [60–69]. Apparent quantum efficiencies for CO production over the 20 wt% P25@CoAl-LDH estimated around 0.10% under 365 nm irradiation (using a UV band pass filter), orders of magnitude higher than the few values reported for CO_2 photoreduction over 'high performance' heterogeneous photocatalysts such as $ZrOCo/IrO_x$ inorganic polynuclear oxide clusters (0.001% [60]), reduced graphene oxide–amine–titanium dioxide nanocomposites (0.0094% [70]) and $SrNb_2O_6$ nanoplates (0.065% [71]). The apparent quantum efficiency for 20 wt% P25@CoAl-LDH of 0.03% at 475 nm (visible band pass filter) is also much higher than recent reports for Fe (0.0013%, [72]) and Ni (0.01% [73]) homogeneous photocatalysts, which also require organic sensitizers or electron donors. Future studies will investigate the impact of titania morphology on nanocomposite physicochemical properties and photocatalytic performance, however preliminary tests show that substituting anatase nanorods [74], for P25 in the synthesis improves CO productivity (Fig. S10) presumably due to their superior charge transport properties and suppressed charge recombination.

Photocatalytic stability of the 20 wt% P25@CoAl-LDH nanocomposite was subsequently explored over three consecutive reactions, in between each of which the catalyst was filtered and washed with water, then replaced in the photoreactor which in turn was charged with fresh deionized water and purged again with CO_2. Around 90% of the original photocatalytic activity was retained after two recycles (Fig. 6d), a key requirement for any practical catalyst, and a common limitation for new photocatalysts [75].

Photocatalytic studies of solar fuel production often utilize a hole scavenger, typically an organic alcohol [76–78], to improve productivity, however such organic scavengers are a potential source of carbon containing products, and hence artefacts, during CO_2 photoreduction. We therefore examined the impact of 2-propanol addition as a hole scavenger during the irradiation of the P25 reference in the absence of CO_2. Significant yields of both gas and liquid phase hydrocarbons (CH_4, C_2H_6, CH_3OH and C_2H_5OH) were observed following 2-propanol addition (Fig. S9)

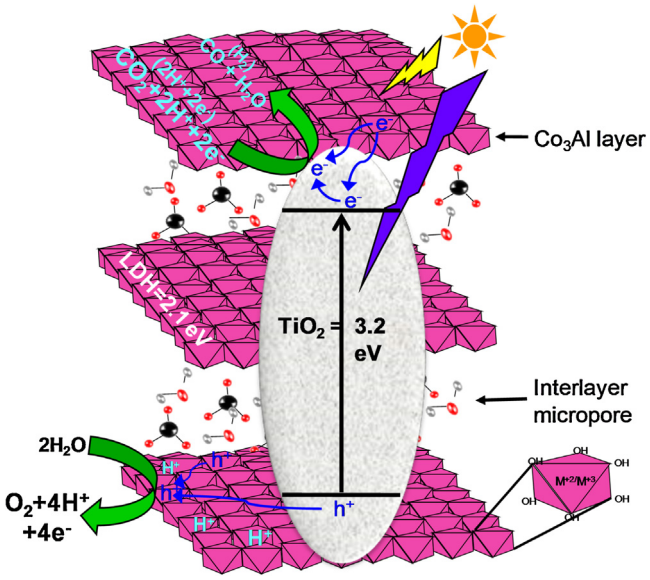

Scheme 2. Proposed mechanism of CO_2 photoreduction due to heterojunction formation within over P25@CoAl-LDH nanocomposite.

which must therefore have arisen from the scavenger. This highlights the importance of adequate control experiments and the exercise of due care in conducting CO_2 photoreduction to eliminate possible contributions from both deliberate organic contaminants (such as scavengers) and accidental organic residues arising from e.g. catalyst precursors and/or solvents used for photoreactor cleaning.

Photocatalytic CO_2 reduction over P25@CoAl-LDH nanocomposites is proposed to occur as follows. Upon visible light irradiation, electrons photoexcited into the conduction band of the CoAl-LDH component (band gap of 2.1 eV) pass across the heterojunction into the conduction band of P25, where CO_2, either weakly chemisorbed directly at the titania surface or spilled over onto titania facets proximate to the basic CoAl-LDH support, undergoes reduction (likely via the $CO_2^{\bullet-}$ anion radical in a proton-coupled process) as illustrated in Scheme 2. In parallel, holes photogenerated in the P25 component (band gap of 3.2 eV) by UV light transfer across the heterojunction into the valence band of CoAl-LDH, where they oxidize chemisorbed water at the LDH surface to liberate dioxygen, with the concomitant protons migrating across the nanojunction interface to P25 and the activated $CO_2^{\bullet-}$ to liberate CO and water.

4. Conclusions

A facile one-pot hydrothermal synthesis of P25@CoAl-LDH nanocomposites is reported, which affords a uniform dispersion of UV photoactive titania nanoparticles throughout a visible light photoactive CoAl-LDH matrix. Attendant formation of a type-II heterojunction between the visible and UV semiconductor components confers enhanced photoinduced charge carrier lifetimes, presumably through spatial separation of photoexcited charge carriers, with electron transfer from the CoAl-LDH to P25 and concomitant reverse hole transfer from P25 to the CoAl-LDH. The resulting P25@CoAl-LDH nanocomposites exhibit a strong synergy between semiconductor components, resulting in excellent activity and selectivity (>90%) under full spectrum irradiation for the aqueous phase photoreduction of CO_2 to CO, with water as the proton source; optimal photoactivity and selectivity occurs for 20 wt% P25 incorporation which likely maximizes the heterojunction interface. These low cost P25@CoAl-LDH nanocomposites also exhibit a good apparent quantum efficiency for CO production, and excellent stability over multiple recycles.

Acknowledgement

We thank the EPSRC (EP/K021796/1 and EP/K029525/2) for financial support.

Appendix A. Supplementary data

Supplementary data associated with this article can be found, in the online version, at http://dx.doi.org/10.1016/j.apcatb.2017.03.006.

References

[1] T. Faunce, S. Styring, M.R. Wasielewski, G.W. Brudvig, A.W. Rutherford, J. Messinger, A.F. Lee, C.L. Hill, H. deGroot, M. Fontecave, D.R. MacFarlane, B. Hankamer, D.G. Nocera, D.M. Tiede, H. Dau, W. Hillier, L. Wang, R. Amal, Artificial photosynthesis as a frontier technology for energy sustainability, Energy Environ. Sci. 6 (2013) 1074–1076.
[2] W. Tu, Y. Zhou, Z. Zou, Photocatalytic conversion of CO2 into renewable hydrocarbon fuels: state-of-the-art accomplishment, challenges, and prospects, Adv. Mater. 26 (2014) 4607–4626.
[3] D. Chen, X. Zhang, A.F. Lee, Synthetic strategies to nanostructured photocatalysts for CO2 reduction to solar fuels and chemicals, J. Mater. Chem. A 3 (2015) 14487–14516.
[4] P.V. Kamat, Meeting the clean energy demand: nanostructure architectures for solar energy conversion, J. Phys. Chem. C 111 (2007) 2834–2860.
[5] M.R. Hoffmann, S.T. Martin, W. Choi, D.W. Bahnemann, Environmental applications of semiconductor photocatalysis, Chem. Rev. 95 (1995) 69–96.
[6] Y.-P. Yuan, L.-W. Ruan, J. Barber, S.C. Joachim Loo, C. Xue, Hetero-nanostructured suspended photocatalysts for solar-to-fuel conversion, Energy Environ. Sci. 7 (2014) 3934–3951.
[7] Y. Ma, X. Wang, Y. Jia, X. Chen, H. Han, C. Li, Titanium dioxide-based nanomaterials for photocatalytic fuel generations, Chem. Rev. 114 (2014) 9987–10043.
[8] K. Nakata, A. Fujishima, TiO2 photocatalysis: design and applications, J. Photochem. Photobiol. C 13 (2012) 169–189.
[9] M. Pelaez, N.T. Nolan, S.C. Pillai, M.K. Seery, P. Falaras, A.G. Kontos, P.S.M. Dunlop, J.W.J. Hamilton, J.A. Byrne, K. O'Shea, M.H. Entezari, D.D. Dionysiou, A review on the visible light active titanium dioxide photocatalysts for environmental applications, Appl. Catal. B 125 (2012) 331–349.
[10] Q. Zhang, D.Q. Lima, I. Lee, F. Zaera, M. Chi, Y. Yin, A highly active titanium dioxide based visible-light photocatalyst with nonmetal doping and plasmonic metal decoration, Angew. Chem. 123 (2011) 7226–7230.
[11] X. Chen, C. Burda, The electronic origin of the visible-Light absorption properties of C-, N- and S-doped TiO2 nanomaterials, J. Am. Chem. Soc. 130 (2008) 5018–5019.
[12] V. Etacheri, M.K. Seery, S.J. Hinder, S.C. Pillai, Highly visible light active tiO2-xNx heterojunction photocatalysts, Chem. Mater. 22 (2010) 3843–3853.
[13] S.N. Habisreutinger, L. Schmidt-Mende, J.K. Stolarczyk, Photocatalytic reduction of CO2 on TiO2 and other semiconductors, Angew. Chem. Int. Ed. 52 (2013) 7372–7408.
[14] G.-S. Li, D.-Q. Zhang, J.C. Yu, A new visible-light photocatalyst: cdS quantum dots embedded mesoporous TiO2, Environ. Sci. Technol. 43 (2009) 7079–7085.
[15] J.S. Jang, H.G. Kim, U.A. Joshi, J.W. Jang, J.S. Lee, Fabrication of CdS nanowires decorated with TiO2 nanoparticles for photocatalytic hydrogen production under visible light irradiation, Int. J. Hydrogen Energy 33 (2008) 5975–5980.
[16] X. Chen, S. Shen, L. Guo, S.S. Mao, Semiconductor-based photocatalytic hydrogen generation, Chem. Rev. 110 (2010) 6503–6570.
[17] H. Zhang, X. Lv, Y. Li, Y. Wang, J. Li, P25-graphene composite as a high performance photocatalyst, ACS Nano 4 (2010) 380–386.
[18] J.L. White, M.F. Baruch, J.E. Pander Iii, Y. Hu, I.C. Fortmeyer, J.E. Park, T. Zhang, K. Liao, J. Gu, Y. Yan, T.W. Shaw, E. Abelev, A.B. Bocarsly, Light-driven heterogeneous reduction of carbon dioxide: photocatalysts and photoelectrodes, Chem. Rev. 115 (2015) 12888–12935.
[19] K. Teramura, S. Iguchi, Y. Mizuno, T. Shishido, T. Tanaka, Photocatalytic conversion of CO2 in water over layered double hydroxides, Angew. Chem. Int. Ed. 51 (2012) 8008–8011.
[20] J. Low, J. Yu, W. Ho, Graphene-Based photocatalysts for CO2 reduction to solar fuel, J. Phys. Chem. Lett. 6 (2015) 4244–4251.
[21] Y. Zhao, F. Li, R. Zhang, D.G. Evans, X. Duan, Preparation of layered double-hydroxide nanomaterials with a uniform crystallite size using a new method involving separate nucleation and aging steps, Chem. Mater. 14 (2002) 4286–4291.
[22] Q. Wang, D. O'Hare, Recent advances in the synthesis and application of layered double hydroxide (LDH) nanosheets, Chem. Rev. 112 (2012) 4124–4155.

[23] L. Mohapatra, K. Parida, A review on the recent progress, challenges and perspective of layered double hydroxides as promising photocatalysts, J. Mat. Chem. A 4 (2016) 10744–10766.
[24] J.L. Gunjakar, T.W. Kim, H.N. Kim, I.Y. Kim, S.-J. Hwang, Mesoporous layer-by-layer ordered nanohybrids of layered double hydroxide and layered metal oxide: highly active visible light photocatalysts with improved chemical stability, J. Am. Chem. Soc. 133 (2011) 14998–15007.
[25] Y. Zhao, M. Wei, J. Lu, Z.L. Wang, X. Duan, Biotemplated hierarchical nanostructure of layered double hydroxides with improved photocatalysis performance, ACS Nano 3 (2009) 4009–4016.
[26] Y. Zhao, X. Jia, G.I.N. Waterhouse, L.-Z. Wu, C.-H. Tung, D. O'Hare, T. Zhang, Layered double hydroxide nanostructured photocatalysts for renewable energy production, Adv. Energy Mater. 6 (2016), 1501974-n/a.
[27] S.-M. Xu, T. Pan, Y.-B. Dou, H. Yan, S.-T. Zhang, F.-Y. Ning, W.-Y. Shi, M. Wei, Theoretical and experimental study on MIIMIII-layered double hydroxides as efficient photocatalysts toward oxygen evolution from water, J. Phys. Chem. C 119 (2015) 18823–18834.
[28] S. Liu, N. Zhang, Z.-R. Tang, Y.-J. Xu, Synthesis of one-dimensional CdS@TiO2 core–shell nanocomposites photocatalyst for selective redox: the dual role of TiO2 shell, ACS Appl. Mater. Interfaces 4 (2012) 6378–6385.
[29] X. Li, H. Lin, X. Chen, H. Niu, J. Liu, T. Zhang, F. Qu, Dendritic [small alpha]-Fe2O3/TiO2 nanocomposites with improved visible light photocatalytic activity, PCCP 18 (2016) 9176–9185.
[30] Y. Dou, S. Zhang, T. Pan, S. Xu, A. Zhou, M. Pu, H. Yan, J. Han, M. Wei, D.G. Evans, X. Duan, TiO2@Layered double hydroxide core–shell nanospheres with largely enhanced photocatalytic activity toward O2 generation, Adv. Funct. Mater. 25 (2015) 2243–2249.
[31] E.M. Seftel, M. Mertens, P. Cool, The influence of the Ti4+ location on the formation of self-assembled nanocomposite systems based on TiO2 and Mg/Al-LDHs with photocatalytic properties, Appl. Catal. B 134–135 (2013) 274–285.
[32] E.M. Seftel, M. Niarchos, C. Mitropoulos, M. Mertens, E.F. Vansant, P. Cool, Photocatalytic removal of phenol and methylene-blue in aqueous media using TiO2@LDH clay nanocomposites, Catal. Today 252 (2015) 120–127.
[33] R. Lu, X. Xu, J. Chang, Y. Zhu, S. Xu, F. Zhang, Improvement of photocatalytic activity of TiO2 nanoparticles on selectively reconstructed layered double hydroxide, Appl. Catal. B 111–112 (2012) 389–396.
[34] L. Shao, Y. Yao, S. Quan, H. Wei, R. Wang, Z. Guo, One-pot in situ synthesized TiO2/layered double hydroxides (LDHs) composites toward environmental remediation, Mater. Lett. 114 (2014) 111–114.
[35] Y.Y. Du, Q. Jin, J.T. Feng, N. Zhang, Y.F. He, D.Q. Li, Flower-like Au/Ni-Al hydrotalcite with hierarchical pore structure as a multifunctional catalyst for catalytic oxidation of alcohol, Catal. Sci. Technol. 5 (2015) 3216–3225.
[36] B.D. Viezbicke, S. Patel, B.E. Davis, D.P. Birnie, Evaluation of the Tauc method for optical absorption edge determination: ZnO thin films as a model system, Phys. Status Solidi B 252 (2015) 1700–1710.
[37] S. Kumar, C.M.A. Parlett, M.A. Isaacs, D.V. Jowett, R.E. Douthwaite, M.C.R. Cockett, A.F. Lee, Facile synthesis of hierarchical Cu2O nanocubes as visible light photocatalysts, Appl. Catal. B 189 (2016) 226–232.
[38] G. Wan, L. Yu, X. Peng, G. Wang, X. Huang, H. Zhao, Y. Qin, Preparation and microwave absorption properties of uniform TiO2@C core-shell nanocrystals, RSC Adv. 5 (2015) 77443–77448.
[39] M. Wang, W.-J. Bao, J. Wang, K. Wang, J.-J. Xu, H.-Y. Chen, X.-H. Xia, A green approach to the synthesis of novel Desert rose stone-like nanobiocatalytic system with excellent enzyme activity and stability, Sci. Rep. 4 (2014) 6606.
[40] R. Li, Z. Hu, X. Shao, P. Cheng, S. Li, W. Yu, W. Lin, D. Yuan, Large scale synthesis of NiCo layered double hydroxides for superior asymmetric electrochemical capacitor, Sci. Rep. 6 (2016) 18737.
[41] Q. Wang, X. Zhang, C.J. Wang, J. Zhu, Z. Guo, D. O'Hare, Polypropylene/layered double hydroxide nanocomposites, J. Mat. Chem. 22 (2012) 19113–19121.
[42] X. Shen, L. Zhu, C. Huang, H. Tang, Z. Yu, F. Deng, Inorganic molecular imprinted titanium dioxide photocatalyst: synthesis, characterization and its application for efficient and selective degradation of phthalate esters, J. Mat. Chem. 19 (2009) 4843–4851.
[43] K.S.W. Sing, D.H. Everett, R.A.W. Haul, L. Moscou, R.A. Pierotti, J. Rouquerol, T. Siemieniewska, Reporting physisorption data for Gas/Solid systems, in: Handbook of Heterogeneous Catalysis, Wiley-VCH Verlag GmbH & Co. KGaA, 2008.
[44] Y. Zhao, S. Zhang, B. Li, H. Yan, S. He, L. Tian, W. Shi, J. Ma, M. Wei, D.G. Evans, X. Duan, A family of visible-Light responsive photocatalysts obtained by dispersing CrO6 octahedra into a hydrotalcite matrix, Chem. Eng. J. 17 (2011) 13175–13181.
[45] J.M. Frost, K.L.M. Harriman, M. Murugesu, The rise of 3-d single-ion magnets in molecular magnetism: towards materials from molecules? Chem. Sci. 7 (2016) 2470–2491.
[46] K. Das, S.N. Sharma, M. Kumar, S.K. De, Morphology dependent luminescence properties of Co doped TiO2 nanostructures, J. Phys. Chem. C 113 (2009) 14783–14792.
[47] P. Li, P.-P. Huang, F.-F. Wei, Y.-B. Sun, C.-Y. Cao, W.-G. Song, Monodispersed Pd clusters generated in situ by their own reductive support for high activity and stability in cross-coupling reactions, J. Mat. Chem. A 2 (2014) 12739–12745.
[48] S. Lee, I.-S. Cho, J.H. Lee, D.H. Kim, D.W. Kim, J.Y. Kim, H. Shin, J.-K. Lee, H.S. Jung, N.-G. Park, K. Kim, M.J. Ko, K.S. Hong, Two-step sol-gel method-Based TiO2 nanoparticles with uniform morphology and size for efficient photo-energy conversion devices, Chem. Mater. 22 (2010) 1958–1965.
[49] W. He, R. Wang, L. Zhang, J. Zhu, X. Xiang, F. Li, Enhanced photoelectrochemical water oxidation on a BiVO4 photoanode modified with multi-functional layered double hydroxide nanowalls, J. Mat. Chem. A 3 (2015) 17977–17982.
[50] T.D. Veal, P.D.C. King, S.A. Hatfield, L.R. Bailey, C.F. McConville, B. Martel, J.C. Moreno, E. Frayssinet, F. Semond, J. Zúñiga-Pérez, Valence band offset of the ZnO/AlN heterojunction determined by x-ray photoemission spectroscopy, Appl. Phys. Lett. 93 (2008) 202108.
[51] Y.S. Lee, D. Chua, R.E. Brandt, S.C. Siah, J.V. Li, J.P. Mailoa, S.W. Lee, R.G. Gordon, T. Buonassisi, Atomic layer deposited gallium oxide buffer layer enables 1.2 V open-circuit voltage in cuprous oxide solar cells, Adv. Mater. 26 (2014) 4704–4710.
[52] K. Selvam, M. Swaminathan, Nano N-TiO2 mediated selective photocatalytic synthesis of quinaldines from nitrobenzenes, RSC Adv. 2 (2012) 2848–2855.
[53] S. Kumar, K. Asokan, R.K. Singh, S. Chatterjee, D. Kanjilal, A.K. Ghosh, Investigations on structural and optical properties of ZnO and ZnO:Co nanoparticles under dense electronic excitations, RSC Adv. 4 (2014) 62123–62131.
[54] R.C. Pawar, S. Kang, J.H. Park, J. -h. Kim, S. Ahn, C.S. Lee, Room-temperature synthesis of nanoporous 1D microrods of graphitic carbon nitride (g-C3N4) with highly enhanced photocatalytic activity and stability, Sci. Rep. 6 (2016) 31147.
[55] D. k. Padhi, K. Parida, S.K. Singh, Facile fabrication of RGO/N-GZ mixed oxide nanocomposite for efficient hydrogen production under visible light, J. Phys. Chem. C 119 (2015) 6634–6646.
[56] J. Sun, H. Zhang, L.-H. Guo, L. Zhao, Two-Dimensional interface engineering of a titania–graphene nanosheet composite for improved photocatalytic activity, ACS Appl. Mater. Interfaces 5 (2013) 13035–13041.
[57] Y. Yu, Y. Tang, J. Yuan, Q. Wu, W. Zheng, Y. Cao, Fabrication of N-TiO2/InBO3 heterostructures with enhanced visible photocatalytic performance, J. Phys. Chem. C 118 (2014) 13545–13551.
[58] S. Nayak, L. Mohapatra, K. Parida, Visible light-driven novel g-C3N4/NiFe-LDH composite photocatalyst with enhanced photocatalytic activity towards water oxidation and reduction reaction, J. Mat. Chem. A 3 (2015) 18622–18635.
[59] C.-C. Yang, Y.-H. Yu, B. van der Linden, J.C.S. Wu, G. Mul, Artificial photosynthesis over crystalline tiO2-based catalysts: fact or fiction? J. Am. Chem. Soc. 132 (2010) 8398–8406.
[60] W. Kim, G. Yuan, B.A. McClure, H. Frei, Light induced carbon dioxide reduction by water at binuclear ZrOCoII unit coupled to Ir oxide nanocluster catalyst, J. Am. Chem. Soc. 136 (2014) 11034–11042.
[61] E. Pastor, F.M. Pesci, A. Reynal, A.D. Handoko, M. Guo, X. An, A.J. Cowan, D.R. Klug, J.R. Durrant, J. Tang, Interfacial charge separation in Cu2O/RuOx as a visible light driven CO2 reduction catalyst, PCCP 16 (2014) 5922–5926.
[62] G. Yin, M. Nishikawa, Y. Nosaka, N. Srinivasan, D. Atarashi, E. Sakai, M. Miyauchi, Photocatalytic carbon dioxide reduction by copper oxide nanocluster-grafted niobate nanosheets, ACS Nano 9 (2015) 2111–2119.
[63] S. Shoji, G. Yin, M. Nishikawa, D. Atarashi, E. Sakai, M. Miyauchi, Photocatalytic reduction of CO2 by CuxO nanocluster loaded SrTiO3 nanorod thin film, Chem. Phys. Lett. 658 (2016) 309–314.
[64] C. Zhao, L. Liu, Q. Zhang, J. Wang, Y. Li, Photocatalytic conversion of CO2 and H2O to fuels by nanostructured Ce-TiO2/SBA-15 composites, Catal. Sci. Technol. 2 (2012) 2558–2568.
[65] H. Zhou, J. Guo, P. Li, T. Fan, D. Zhang, J. Ye, Leaf-architectured 3D hierarchical artificial photosynthetic system of perovskite titanates towards CO2 photoreduction into hydrocarbon fuels, Sci. Rep. 3 (2013) 1667.
[66] C. Wang, R.L. Thompson, P. Ohodnicki, J. Baltrus, C. Matranga, Size-dependent photocatalytic reduction of CO2 with PbS quantum dot sensitized TiO2 heterostructured photocatalysts, J. Mat. Chem. 21 (2011) 13452–13457.
[67] C. Zhao, L. Liu, G. Rao, H. Zhao, L. Wang, J. Xu, Y. Li, Synthesis of novel MgAl layered double oxide grafted TiO2 cuboids and their photocatalytic activity on CO2 reduction with water vapor, Catal. Sci. Technol. 5 (2015) 3288–3295.
[68] H. Zhou, P. Li, J. Guo, R. Yan, T. Fan, D. Zhang, J. Ye, Artificial photosynthesis on tree trunk derived alkaline tantalates with hierarchical anatomy: towards CO2 photo-fixation into CO and CH4, Nanoscale 7 (2015) 113–120.
[69] L. He, T.E. Wood, B. Wu, Y. Dong, L.B. Hoch, L.M. Reyes, D. Wang, C. Kübel, C. Qian, J. Jia, K. Liao, P.G. O'Brien, A. Sandhel, J.Y.Y. Loh, P. Szymanski, N.P. Kherani, T.C. Sum, C.A. Mims, G.A. Ozin, Spatial separation of charge carriers in In2O3–x(OH)y nanocrystal superstructures for enhanced gas-phase photocatalytic activity, ACS Nano. 10 (2016) 5578–5586.
[70] Y. Nie, W.-N. Wang, Y. Jiang, J. Fortner, P. Biswas, Crumpled reduced graphene oxide-amine-titanium dioxide nanocomposites for simultaneous carbon dioxide adsorption and photoreduction, Catal. Sci. Technol. 6 (2016) 6187–6196.
[71] S. Xie, Y. Wang, Q. Zhang, W. Deng, Y. Wang, SrNb2O6 nanoplates as efficient photocatalysts for the preferential reduction of CO2 in the presence of H2O, Chem. Commun. 51 (2015) 3430–3433.
[72] J. Bonin, M. Robert, M. Routier, Selective and efficient photocatalytic CO2 reduction to CO using visible light and an iron-based homogeneous catalyst, J. Am. Chem. Soc. 136 (2014) 16768–16771.
[73] V.S. Thoi, N. Kornienko, C.G. Margarit, P. Yang, C.J. Chang, Visible-light photoredox catalysis: selective reduction of carbon dioxide to carbon monoxide by a nickel N-heterocyclic carbene–isoquinoline complex, J. Am. Chem. Soc. 135 (2013) 14413–14424.
[74] J. Chen, H.B. Yang, J. Miao, H.-Y. Wang, B. Liu, Thermodynamically driven one-dimensional evolution of anatase TiO2 nanorods: one-step hydrothermal

synthesis for emerging intrinsic superiority of dimensionality, J. Am. Chem. Soc. 136 (2014) 15310–15318.
[75] S. Kumar, T. Surendar, A. Baruah, V. Shanker, Synthesis of a novel and stable g-C3N4-Ag3PO4 hybrid nanocomposite photocatalyst and study of the photocatalytic activity under visible light irradiation, J. Mater. Chem. A 1 (2013) 5333–5340.
[76] G.R. Dey, A.D. Belapurkar, K. Kishore, Photo-catalytic reduction of carbon dioxide to methane using TiO2 as suspension in water, J. Photochem. Photobiol. A 163 (2004) 503–508.
[77] W. Tu, Y. Zhou, Q. Liu, S. Yan, S. Bao, X. Wang, M. Xiao, Z. Zou, An in situ simultaneous reduction-hydrolysis technique for fabrication of tiO2-graphene 2D sandwich-like hybrid nanosheets: graphene-promoted selectivity of photocatalytic-driven hydrogenation and coupling of CO2 into methane and ethane, Adv. Funct. Mater. 23 (2013) 1743–1749.
[78] H. Park, H.-H. Ou, U. Kang, J. Choi, M.R. Hoffmann, Photocatalytic conversion of carbon dioxide to methane on TiO2/CdS in aqueous isopropanol solution, Catal. Today 266 (2016) 153–159.